Jurnal Kejuruteraan 38(7) 2026: 3173-3184
https://doi.org/10.17576/jkukm-2026-38(7)-01

Comparative Study on the Structural and Compositional Analysis of Hydroxyapatite (HA) Synthesized from *Corbicula Fluminea* and *Pholas Orientalis* Shells under Different Synthesis Parameters

Mohd Riza Mohd Roslan[a*], Nashrul Fazli Mohd Nasir[b], Nur Farahiyah Mohamad[b] & Mohd Ikmar Nizam Isa[a]

[a]*Health Industry Technology Programme, Faculty of Science and Technology, Universiti Sains Islam Malaysia, Nilai 71800, Malaysia*

[b]*Faculty of Electronic Engineering and Technology, Universiti Malaysia Perlis, 02600 Arau, Perlis, Malaysia*

[*]*Corresponding author: rizaroslan@usim.edu.my*

Received 28 October 2025, Received in revised form 15 July 2026
Accepted 15 August 2026, Available online 30 October 2026

ABSTRACT

The utilization of shell-derived hydroxyapatite (HA) as a sustainable biomaterial has gained increasing attention however, comparative studies involving different shell sources and synthesis conditions remain limited. This study investigated the effects of shell source, reaction pH and sintering treatment on the structural, compositional and morphological properties of HA synthesized from Corbicula Fluminea and Pholas Orientalis shells using a chemical precipitation method. HA samples were prepared at pH 10 and pH 11, with and without sintering at 500°C and characterized using Fourier Transform Infrared (FTIR) spectroscopy, X-ray Diffraction (XRD), Field Emission Scanning Electron Microscopy (FESEM) and Energy Dispersive X-ray (EDX) spectroscopy. FTIR analysis confirmed the successful formation of HA and revealed stronger carbonate substitution in Pholas Orientalis-derived samples, indicating the presence of type-B carbonated HA. XRD results showed that all synthesized samples exhibited the characteristic hexagonal HA phase with crystallite sizes ranging from 4.20 to 15.47 nm. HA derived from Pholas Orientalis exhibited slightly lower crystallinity (41.70%) compared to Corbicula Fluminea-derived HA (44.95%). FESEM observations demonstrated that increasing the synthesis pH from 10 to 11 produced finer and more homogeneous particles, while sintering promoted particle densification and crystal growth. EDX analysis revealed Ca/P ratios of 1.42-1.51 for Corbicula Fluminea-derived HA and 1.59-2.13 for Pholas Orientalis-derived HA. The findings indicate that shell source and synthesis parameters significantly influence HA characteristics and can be tailored to develop sustainable biomaterials for bone tissue engineering and other biomedical applications.

Keywords: Hydroxyapatite; Corbicula Fluminea; Pholas Orientalis; structural and compositional analysis

INTRODUCTION

Hydroxyapatite (HA) with the molecular formula of $Ca_{10}(PO_4)_6(OH)_2$ (Bernache-Assollant et al. 2003) crystallizes in a hexagonal system under the $P6_3/m$ space group. The lattice constants of HA for a = b = 0.9418 nm and c = 0.6884 nm (Guerfi et al. 2024) with a stoichiometric Ca/P molar ratio of 1.67 (Zhang et al. 2022). HA constitutes the predominant inorganic phase in the mineralized matrix of human bone tissue. HA, especially in nanostructured (nHA) form also has wide applications such as bone tissue engineering (Fendi et al. 2024), in dental and oral health (Tao et al. 2022), coatings for biomedical implants (Awasthi et al. 2021) and drug and therapeutic delivery (Lubojański et al. 2024). Few methods in synthesizing HA such as hydrothermal (Karalkeviciene et al. 2023), alkaline hydrolysis (Etinosa et al. 2024), emulsion, sonochemical and combustion/pyrolysis (Alam et al. 2024) but the chemical precipitation method possesses practicality and the ability to produce HA at the nanoscale (Hassanein et al. 2024; Wu et al. 2023). In line with the Sustainable Development Goals (SDGs), a critical review emphasizes the production of biomaterials through green chemistry methods utilizing waste materials, crops or by-products from the food industry (Bontempi et al. 2021). Hence, researchers have focused on natural resources to synthesize biomaterials including the nHA. Some of the natural resources such as eggshells (Noviyanti et al. 2020), fish

bone (Jindapon et al. 2023), snail shells (Ahmed et al. 2022) and seashells from marine sources (Seyhan et al. 2022). Among all the materials listed above, calcium carbonate ($CaCO_3$) is the primary chemical compound extracted as it is abundantly present in these natural resources (Aditya et al. 2021; Owuamanam & Cree 2020; Torres et al. 2024). However, there are also a few trace elements that exist in stated natural resources other than $CaCO_3$ such as magnesium (Mg), sodium (Na) and strontium (Sr) (Hussin et al. 2022). A few clams in Malaysia such as *Corbicula Fluminea* and *Pholas Orientalis* shells showed trace elements such as Sr besides being rich with $CaCO_3$. *Corbicula Fluminea* widely known as the Asian or Asiatic clam is a freshwater bivalve mollusk species originally found in Eastern Asia (Sousa et al. 2008). *Pholas Orientalis*, also known as the angelwing clam, is a marine bivalve mollusk belonging to the *Pholadidae* family. It is commonly found along the coastal areas of Southeast Asia, including Malaysia (Ho et al. 2024).

Corbicula Fluminea and *Pholas Orientalis* shells are both rich sources of $CaCO_3$ however, they differ in form, impurity content, and crystal morphology. The predominant polymorph in *Corbicula Fluminea* shells is aragonite, whereas *Pholas Orientalis* shells primarily consist of calcite (Huang & Zhang 2022). Consequently, synthesizing HA from different $CaCO_3$ sources results in distinct structural and compositional characteristics. Previous studies (Benataya et al. 2020; Golubevas et al. 2020), have shown that the incorporation of other ions such as carbonate (CO_3^{2-}) into the HA lattice markedly influences its crystal structure, morphology and surface area. In addition, the crystallinity of HA is affected by the pH of the reaction mixture during synthesis. For instance, (Kalpana & Nagalakshmi 2023) reported an increase in crystallinity when the pH was raised from pH10 to pH11 (Lee et al. 2020; Sánchez-Campos et al. 2021). Furthermore, the sintering process plays a critical role in determining HA crystallinity with higher sintering temperatures leading to greater crystalline order (Hossain et al. 2021; Trzaskowska et al. 2023).

Crucially, the researcher (Wu et al. 2024) has highlighted the significance of crystallinity in nHA whereby the higher crystallinity releases more Ca^{2+} ions. This in turn enhances cell mineralization, growth and differentiation. The rod-like structure of HA particles also has a great influence on cell adhesion and proliferation. While the low crystallinity of nHA is reported to promote biological behavior when in contact with human mesenchymal stem cells (Ebrahimi et al. 2021). Research conducted by (Benataya et al. 2020) demonstrated that an increase in crystallite size along with a corresponding rise in specific surface area promotes cell proliferation and enhances alkaline phosphatase activity. Both conditions portrayed positive indicators of osteogenic differentiation. In the mechanical aspect, higher crystallinity of HA possessed a better compression strength, Young's modulus and fracture toughness which match the mechanical strength of cortical bone (Liang et al. 2024). Therefore, the crystallinity and morphology of HA particles play a crucial role in biomedical applications as both factors significantly influence the material's bioactivity. To date, there is no comparative study that has been done to measure the structural and compositional properties of HA based on *Corbicula Fluminea* and *Pholas Orientalis* shells since the $CaCO_3$ polymorphs are different for both species. The comparative interaction of both species at different pH values and the sintering process while synthesizing the HA is worth venturing into. Hence, this study is a comparative study that emphasizes several key aspects in evaluating the effects of $CaCO_3$ source type (*Corbicula Fluminea* and *Pholas Orienalis* shells), reaction mixture pH (pH10 and pH 11), and sintering process (sintering at 500°C or without sintering) on the structural and compositional properties of synthesized HA.

METHODOLOGY

SYNTHESIS OF HA POWDER

Corbicula Fluminea and *Pholas Orientalis* shells were collected and further purified. The shells were boiled using distilled water at 100°C to remove the dirt and flesh. The seashells were then dried in the oven at 100°C for 1hour followed by crushing them into powder form by using a grinder. Both compounds are $CaCO_3$ and were transformed into calcium oxide (CaO) by heating at a temperature of 1100°C with a rate of 10°C/min by using a furnace as described in Equation (1).

$$CaCO_3(s) \rightarrow CaO(s) + CO_2(g) \quad (1)$$

The product of CaO in the form of solid powder was then reacted with distilled water as in Equation (2). Specifically, 5g of CaO was reacted with 100ml of distilled water stirred under hot plate at a temperature of 45°C, which is the reaction temperature for 2hours. The product of this reaction is calcium hydroxide ($Ca(OH)_2$).

$$CaO\ (s) + H_2O\ (l) \rightarrow Ca(OH)_2\ (aq) \quad (2)$$

After 2hours, the mixture of $Ca(OH)_2$ was reacted with 2.8ml of phosphoric acid (H_3PO_4) under a titration process. During the titration process, the pH value was monitored and adjusted to pH10 and pH11 for both types of shells (*Corbicula Fluminea* and *Pholas Orientalis* shells) by

using ammonia solution (NH_3). Herewith, the pH value is the manipulated variable of this research. The result of H_3PO_4 titration with $Ca(OH)_2$ is HA as in Equation (3).

$$10Ca(OH)_2 + 6H_3PO_4 \rightarrow Ca_{10}(PO_4)_6(OH)_2 + 18H_2O \quad (3)$$

The HA gelatinous solution formed was aged 24hours at room temperature to allow for complete reaction. After 24hours, the gelatinous solution was poured into a centrifuge tube with distilled water and mixed using a vortex mixer to wash the HA product. This process was repeated 3 times. After washing it, the precipitate formed at the bottom of the centrifuge tube was collected and dried in the oven at 110°C for 6hours. After the heating process, the cake formed was powdered using the mortar and pestle. Some of the HA powder form was then sintered at 500°C (manipulated variable) before undergoing characterization. The sintering temperature of 500°C was selected based on previous studies demonstrating that heat treatment at this temperature improves hydroxyapatite crystallinity, promotes crystal growth and particle densification. Also, it facilitates the removal of residual impurities without significant phase decomposition. Furthermore, 500°C has been reported as a suitable temperature for investigating the combined effects of pH and thermal treatment on the structural and morphological properties of hydroxyapatite (Rodríguez-Lugo et al. 2018; Trzaskowska et al. 2023). All the samples were prepared with different parameters regarding different variables of manipulation as stated in Table 1 for sampling purposes.

TABLE 1. Samples labelling and synthesis parameters

Sample	Types of shells	pH value	Sintering process
HA1	*Corbicula Fluminea*	10	No sintering process
HA2			Sintering at 500°C
HA3		11	No sintering process
HA4			Sintering at 500°C
HA5	*Pholas Orientalis*	10	No sintering process
HA6			Sintering at 500°C
HA7		11	No sintering process
HA8			Sintering at 500°C

CHARACTERIZATION

FOURIER TRANSFORM INFRARED (FTIR) SPECTROSCOPY

FTIR analysis was conducted to identify the functional groups present in the HA powders and confirm HA formation. The study was carried out using a Perkin Elmer Spectrum 65 FTIR spectrometer, operating within the frequency range of 400cm^{-1} to 4000cm^{-1}.

X-RAY DIFFRACTION (XRD) SPECTROSCOPY

The phases and crystallographic structures of the synthesized samples were determined using X-ray diffraction (XRD) analysis with a Bruker D2 Phaser diffractometer. The HA powder was compacted into an XRD sample holder before scanning for sample preparation. The analysis was conducted over a 2θ range of 10° to 90°, with a step size of 0.1° and a scan rate of 5°/min. The resulting XRD patterns were compared against standard powder diffraction files using X'Pert HighScore Plus software (version 2.2.5). The degree of crystalline phase which represents the fraction of the crystalline phase was calculated using Equation (4).

$$\text{Crystallinity phase, } X_C = 1 - \frac{V_{112/300}}{I_{300}} \quad (4)$$

Xc represents the fraction of the crystalline phase, I_{300} refers to the intensity of the (300) reflection, and $V_{112}/_{300}$ indicates the intensity of the hollow between the (112) and (300) diffraction peaks. The crystallite size (Xs) in the direction perpendicular to the crystal plane was estimated using Scherrer's formula, as shown in Equation (5).

$$\text{Crystallite size, } X_S = \frac{k\lambda}{\beta \cos\theta} \quad (5)$$

Xs refers to the crystallite size in nanometres (nm), while λ is the wavelength of the monochromatic X-ray beam, which is 0.15406 nm for CuKα radiation. β, which is equivalent to FWHM stands for the full width at half maximum of the selected diffraction peak measured in radians. For the crystallite size calculation, the diffraction peak at 2θ = 25.88° corresponding to the (002) plane was chosen because it is sharper and well-separated from nearby peaks. Meanwhile, the hexagonal lattice parameters of HA is associated with Equation (6).

$$\frac{1}{d^2} = \frac{4}{3}\left(\frac{h^2 + hk + k^2}{a^2}\right) + \frac{l^2}{c^2} \quad (6)$$

FIELD EMISSION SCANNING ELECTRON MICROSCOPY (FESEM) & ENERGY DISPERSIVE X-RAY (EDX) SPECTROSCOPY

The morphologies of the samples were characterized by a field emission scanning electron microscope, Hitachi with an excitation voltage of 15kV. Before FESEM observation, the sample was prepared by dispersing the powders on a double-sided carbon tape mounted on the aluminum sample holder. Then the sample was coated with a thin Platinum (Pt) layer before observing under FESEM. The elemental composition of the samples was analyzed by using EDX which determined the atomic percentage (at%) and mass percentage (wt%) of each element. The elements Ca, P, C and O were evaluated and six surface scan graphs were obtained for each sample.

RESULTS AND DISCUSSION

FTIR ANALYSIS

Table 2 tabulates the wavenumber of the respective functional group with the vibration mode and Figure 1 shows the FTIR spectrum for all HA samples. All the samples showed the phosphate (PO_4^{3-}) functional groups which are the crucial functional groups for the HA lattice structure. The stretching mode of the hydroxyl (OH-) functional group was also found in all HA samples, confirming the stoichiometric HA structures. CO_3^{2-} functional groups were found in all the HA samples but were different in terms of intensity. Analyzing the peaks from HA1 to HA8, the peaks at 960cm^{-1} and 1020cm^{-1} showed a progressively intensified peak suggesting the sample has better crystallinity or better phase purity. The peak splitting within 1020cm^{-1} - 1090cm^{-1} is getting obvious especially for the HA5, HA6, HA7 and HA8 samples. This suggests more than one of the PO_4^{3-} structures exists due to the presence of the secondary phase.

Analyzing the FTIR spectrum based on the different sources of $CaCO_3$ (*Corbicula Fluminea* and *Pholas Orientalis* shells), HA5, HA6, HA7 and HA8 which is based on *Pholas Orientalis* shell showed a higher intensity of CO_3^{2-} peaks at 870cm^{-1} and 1410cm^{-1} to 1450cm^{-1} compared to HA1, HA2, HA3 and HA4 (HA based *Corbicula Fluminea* shell). Both types of HA which are based on different sources of $CaCO_3$ (*Corbicula Fluminea* and *Pholas Orientalis* shells) presented at CO_3^{2-} peaks but these peaks are more prominent in HA based on *Pholas Orientalis* shell. These peaks portrayed the PO_4^{3-} which was substituted by CO_3^{2-} in the HA structure (Mohd Noor et al. 2020). Hence, it is suggested that the HA samples from *Pholas Orientalis* shell are more likely to be classified as type-B carbonated HA. The carbonated HA type-B closely resembles the biological apatite of bone tissue which is composed of 4-6% carbonate by weight (Liu et al. 2021).

TABLE 2. Functional groups present in HA samples

Wavenumber (cm^{-1})	Vibration mode	Functional group	Reference
960	v_1 symmetric stretching	Phosphate (PO_4^{3-})	(Ebrahimi et al. 2021)
1020-1090	v_3 asymmetric stretching	Phosphate (PO_4^{3-})	(Ebrahimi et al. 2021)
3570	stretching mode	Hydroxyl (OH^-)	(Ebrahimi et al. 2021)
870	out of plane bending v_2	Carbonate (CO_3^{2-})	(Liang et al. 2024)
1410-1465	asymmetric stretching v_3	Carbonate (CO_3^{2-})	(Liang et al. 2024)

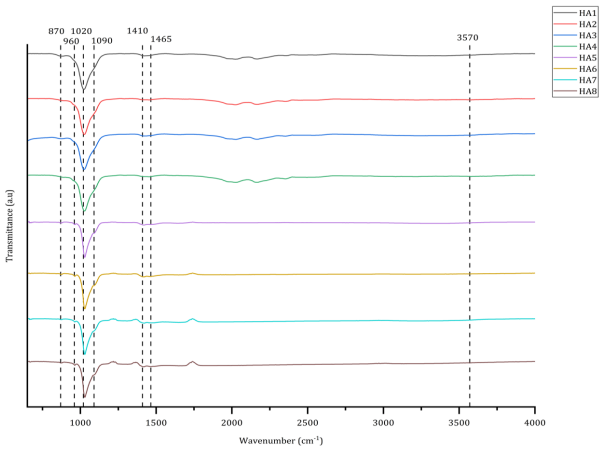


FIGURE 1. FTIR spectrum for synthesized HA

Assessing the significance of different pH values in synthesizing HA for both types of $CaCO_3$ sources (*Corbicula Fluminea* and *Pholas Orientalis* shell), it showed a similar trend. Samples that were synthesized at pH10 are HA1, HA2, HA5 and HA6. While samples that were synthesized at pH11 are HA3, HA4, HA7 and HA8. HA samples that were synthesized at pH11 showed a slight increase in PO_4^{3-} peak sharpness at wavelengths 1020cm^{-1} to 1090cm^{-1}. The increasingly sharp PO_4^{3-} peaks depict that the peaks have greater crystallinity with lesser substitution of CO_3^{2-} ions. The lesser CO_3^{2-} ions in the HA lattice are confirmed by the CO_3^{2-} peaks at 870cm^{-1} and 1450cm^{-1} being nearly absent at pH11. Theoretically, at higher pH

levels, fewer free CO_3^{2-} ions are present because carbon dioxide (CO_2) from the surroundings interacts less with the synthesis solution, as CO_2 becomes less soluble at elevated pH (Nowicki et al. 2022).

Scrutinizing the significance of sintering effects, regardless of the HA based on $CaCO_3$ sources (*Corbicula Fluminea* and *Pholas Orientalis* shells), samples that were sintered at 500°C (HA2, HA4, HA6 and HA8) showed a sharper and more intense PO_4^{3-} peak which can be found at 1020cm^{-1} – 1090cm^{-1}. On the other hand, CO_3^{2-} peaks at 870cm^{-1} and 1450cm^{-1} especially for HA2 and HA4 samples showed a decrement trend. It also noted that there is a slight appearance or sharpening of OH^- functional group peak at 3570cm^{-1} for the sintered samples.

XRD ANALYSIS

The XRD pattern in Figure 2 shows the diffraction profiles of the synthesized HA samples within the measurement range of $10° < 2\theta < 60°$. The diffraction peaks observed at 2θ values of 25.90°, 31.77°, 32.90°, 32.19°, 34.05°, 39.82°, 46.71°, 49.49°, and 53.20° correspond to the (002), (211), (112), (300), (202), (310), (222), (213), and (004) crystallographic planes of HA respectively in agreement with PDF 01-074-0565. The absence of significant secondary phase peaks indicates that all synthesized samples predominantly consisted of the hexagonal HA phase. Notably, although HA8 exhibited a relatively high Ca/P ratio of 2.13 according to EDX analysis (analysed in the next subtopic), no distinct diffraction peaks corresponding to secondary calcium-containing phases such as CaO or $CaCO_3$ were detected. This suggests that any excess calcium species were either present below the detection limit of XRD or existed as non-crystalline/ calcium-rich regions without forming a separate crystalline phase. Table 3 summarizes the lattice parameters, crystallite sizes, and crystallinity values obtained from the XRD analysis.

Comparing the HA samples synthesized from different $CaCO_3$ sources, HA derived from *Corbicula Fluminea* shells (HA1–HA4) exhibited crystallinity values ranging from 38.03% to 51.10%, with an average crystallinity of 44.95%. In contrast, HA derived from *Pholas Orientalis* shells (HA5–HA8) showed crystallinity values between 36.74% and 51.47%, with an average crystallinity of 41.70%. These results indicate that both shell sources produced moderately crystalline HA with only slight differences in overall crystallinity. Meanwhile, the crystallite sizes of HA derived from *Corbicula Fluminea* shells ranged from 4.20nm to 15.47nm which were generally larger than those obtained from *Pholas Orientalis* shells (4.61nm to 7.82nm). The $CaCO_3$ source therefore appears to exert a greater influence on crystallite growth than on the degree of crystallinity. This behaviour may be attributed to differences in shell microstructure, mineral arrangement, hierarchical architecture and precursor composition which influence nucleation and crystal growth during HA formation.

Based on the lattice parameters result, the a-lattice parameter for HA synthesized from *Corbicula Fluminea* shells ranged from 0.874nm to 0.902nm whereas the corresponding values for *Pholas Orientalis* shells ranged from 0.903nm to 0.904nm. Similarly, the c-lattice parameter ranged from 0.677nm to 0.687nm for *Corbicula Fluminea*-derived HA and from 0.680nm to 0.682nm for *Pholas Orientalis*-derived HA. On average, the lattice parameters of HA synthesized from *Pholas Orientalis* shells were slightly closer to the ideal hexagonal HA structure. The relatively larger deviation observed in some *Corbicula Fluminea*-derived samples particularly HA3, may be associated with CO_3^{2-} substitution, crystallite size effects, crystal defects and structural disorder arising from the natural shell precursor.

A comparison between FTIR and XRD analyses reveals an interesting observation. FTIR results showed stronger CO_3^{2-} absorption bands for HA synthesized from *Pholas Orientalis* shells, suggesting greater CO_3^{2-} incorporation into the HA structure. Since CO_3^{2-} substitution is commonly associated with reduced crystallinity due to lattice distortion, a lower crystallinity would normally be expected. However, the XRD results demonstrated that the *Pholas Orientalis*-derived HA maintained comparable crystallinity to the *Corbicula Fluminea*-derived samples. This apparent discrepancy can be explained by the different sensitivities of the two characterization techniques. FTIR is highly sensitive to vibrational modes of CO_3^{2-} species, including surface-adsorbed and amorphous CO_3^{2-} whereas XRD evaluates the long-range atomic ordering of the crystal lattice. Consequently, CO_3^{2-} species detected by FTIR may not be present in sufficient quantities to significantly disrupt the crystalline HA framework detected by XRD.

The pH value also influenced the structural characteristics of the synthesized HA. Samples synthesized at pH10 (HA1, HA2, HA5, and HA6) exhibited an average crystallinity of 43.96%, while samples synthesized at pH11 (HA3, HA4, HA7, and HA8) showed a slightly lower average crystallinity of 42.69%. Although the difference is relatively small, the results suggest that increasing the pH from pH10 to pH11 did not markedly improve crystallinity under the present synthesis conditions. In contrast, the average crystallite size increased from 5.48nm at pH10 to 8.03nm at pH11 indicating that a more alkaline environment promoted crystal growth. The a-lattice

parameter ranged from 0.901nm to 0.904nm and the c-lattice parameter from 0.677nm to 0.682nm for pH10 samples. For pH11 samples, the a-lattice parameter ranged from 0.874nm to 0.904nm while the c-lattice parameter ranged from 0.679nm to 0.687nm. Notably, HA3 (pH 11 without sintering) exhibited a contracted a-lattice parameter of 0.874nm, suggesting lattice distortion. This observation indicates that synthesis at higher pH may induce structural instability in the absence of subsequent heat treatment. The additional OH^- ions present at higher alkalinity may contribute to ionic disorder whereas thermal treatment restores lattice stability and produces lattice parameters closer to those of stoichiometric HA.

The crystallinity trends obtained from XRD are consistent with the FTIR findings. Samples exhibiting more pronounced CO_3^{2-} substitution particularly type-B carbonated HA where CO_3^{2-} ions substitute for PO_4^{3-} ions generally showed slightly lower crystallinity because CO_3^{2-} incorporation introduces structural disorder into the HA lattice. This effect was more evident in non-sintered samples and in samples synthesized at higher pH without thermal treatment. Conversely, the reduction of CO_3^{2-} related features following heat treatment contributed to improved lattice ordering and enhanced crystallinity.

Examining the effect of sintering, all sintered samples (HA2, HA4, HA6, and HA8) exhibited higher crystallinity and larger crystallite sizes compared with their non-sintered counterparts. The average crystallinity increased from 40.52% for non-sintered samples to 46.13% after sintering, while the average crystallite size increased from 4.53nm to 8.97nm. The enhancement in crystallinity can be attributed to thermally induced crystal growth, reduction of lattice defects and improved atomic ordering within the HA structure. The thermal energy supplied during sintering promotes densification and grain coalescence allowing smaller crystallites to combine into larger and more ordered crystal domains. This phenomenon was particularly evident in HA2 and HA8, which recorded the highest crystallinity values of 51.10% and 51.47%, respectively. Furthermore, the lattice parameters of the sintered samples approached the ideal HA values, with a-lattice parameters ranging from 0.900nm to 0.904nm and c-lattice parameters close to 0.680nm to 0.682nm.

The FTIR results further supported the XRD observations. Non-sintered samples displayed stronger CO_3^{2-} absorption bands, whereas these bands weakened after sintering. Simultaneously, the PO_4^{3-} and OH^- absorption bands became sharper and more prominent indicating improved phase purity and crystallinity. Overall, the XRD analysis demonstrates that both shell-derived $CaCO_3$ sources are suitable precursors for HA synthesis while the sintering process exerts the most significant influence on crystallite growth, lattice ordering and crystallinity enhancement.

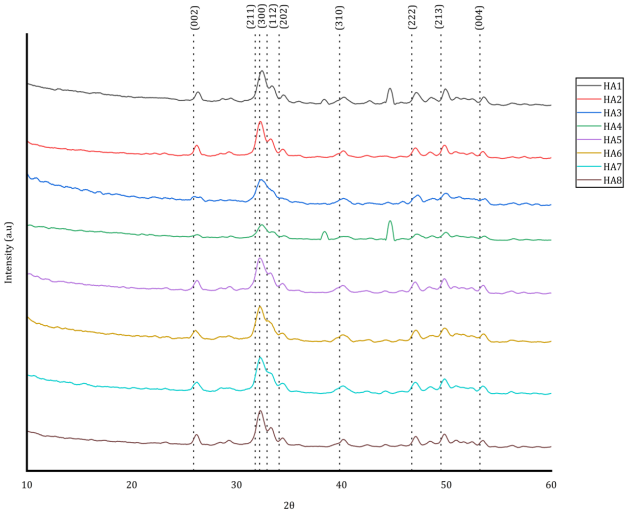


FIGURE 2. XRD pattern for synthesized HA

TABLE 3. The XRD information of HA samples

Sample	Lattice parameter (nm)		Crystallite size, X_s (nm)	Crystallinity, X_c (%)
	a	c		
HA1	0.901	0.677	4.681	46.14
HA2	0.902	0.680	7.926	51.10
HA3	0.874	0.687	4.204	38.03
HA4	0.900	0.679	15.468	44.52
HA5	0.903	0.680	4.644	41.16
HA6	0.904	0.682	4.683	37.44
HA7	0.904	0.680	4.608	36.74
HA8	0.903	0.681	7.822	51.47

FESEM ANALYSIS

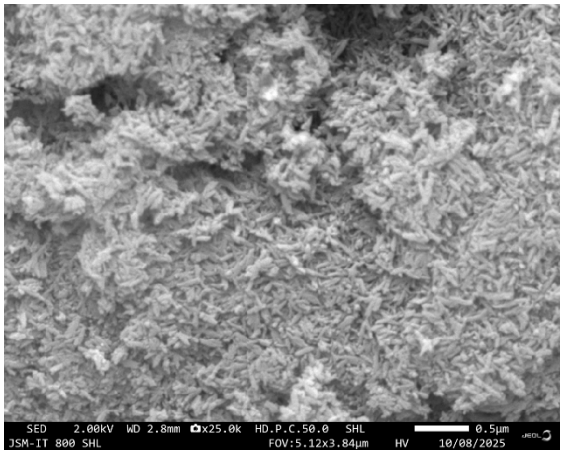
The surface morphologies of the synthesized HA derived from *Corbicula Fluminea* and *Pholas Orientalis* shells under different synthesis conditions were examined using FESEM, as presented in Figure 3(a–h). All samples exhibited the characteristic rod-like or rice-like morphology associated with precipitation-derived HA. To quantitatively evaluate the morphological differences observed in the FESEM images, the lengths of 30 randomly selected particles were measured for each sample and the mean particle lengths together with their standard deviations are summarized in Table 4.

For the HA samples derived from *Corbicula Fluminea* shells (HA1–HA4), the non-sintered sample synthesized at pH10 (HA1) exhibited loosely packed particles with an average particle length of 174.568µm ± 23.139µm. After

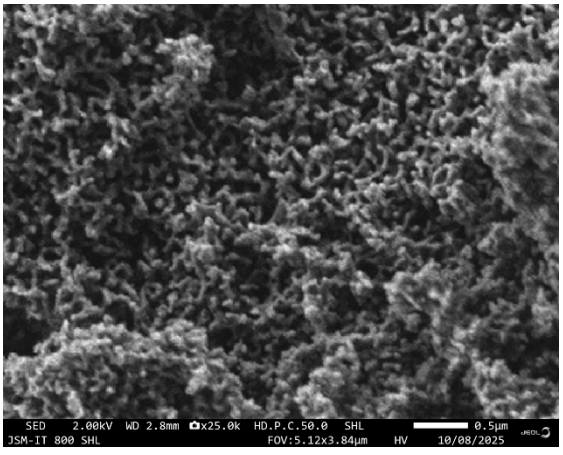
sintering at 500°C (HA2), the average particle length decreased to 111.176µm ± 28.462µm accompanied by increased particle densification and grain fusion. Increasing the synthesis pH to pH11 without sintering (HA3) produced more uniformly distributed rod-like particles with an average length of 116.870µm ± 36.500µm. The combination of pH11 and sintering at 500°C (HA4) further reduced the average particle length to 95.046µm ± 31.258µm which indicates improved particle refinement and microstructural uniformity.

A similar trend was observed for HA derived from *Pholas Orientalis* shells (HA5–HA8). The non-sintered sample synthesized at pH 10 (HA5) exhibited an irregular morphology with an average particle length of 91.795µm ± 21.879µm. Upon sintering at 500°C (HA6), crystal growth and particle coalescence became more apparent, resulting in a larger average particle length of 170.497µm ± 31.007µm. When synthesized at pH11 without sintering (HA7), the smallest average particle length among all samples was obtained (72.159µm ± 21.581µm) indicating the formation of finer particles. After sintering at 500°C (HA8), the particle length increased to 121.212µm ± 35.098µm, together with the development of a denser and more compact microstructure.

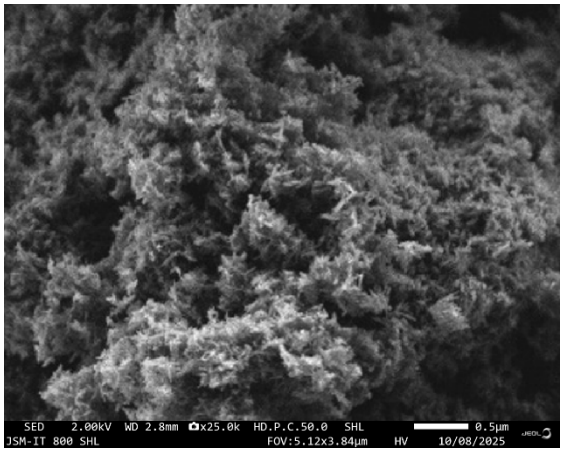
Overall, the quantitative particle size measurements support the qualitative FESEM observations. Increasing the synthesis pH from pH10 to pH11 generally reduced the average particle length for both shell sources. For example, particle length decreased by approximately 33.0% from HA1 to HA3 and by 21.4% from HA5 to HA7. The formation of finer particles at higher pH suggests that increased alkalinity enhanced nucleation kinetics, generating a greater number of nuclei and restricting excessive crystal growth. Furthermore, the lower average particle size observed for HA7 (72.159µm ± 21.581µm) compared with HA1 (174.568µm ± 23.139µm) confirms that higher pH favors the formation of finer HA particles. The relatively lower standard deviations observed for HA5 and HA7 also indicate a narrower particle size distribution and improved particle homogeneity. These findings quantitatively validate the observed FESEM morphology and demonstrate that both pH and sintering conditions significantly influence the microstructural evolution of shell-derived HA.



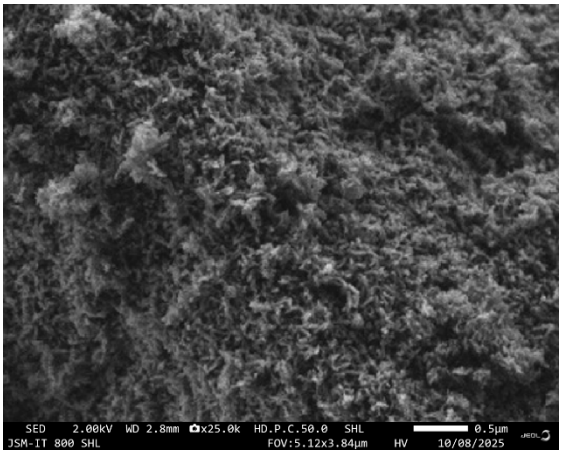
(a)



(b)



(c)



(d)

continue...

...cont.

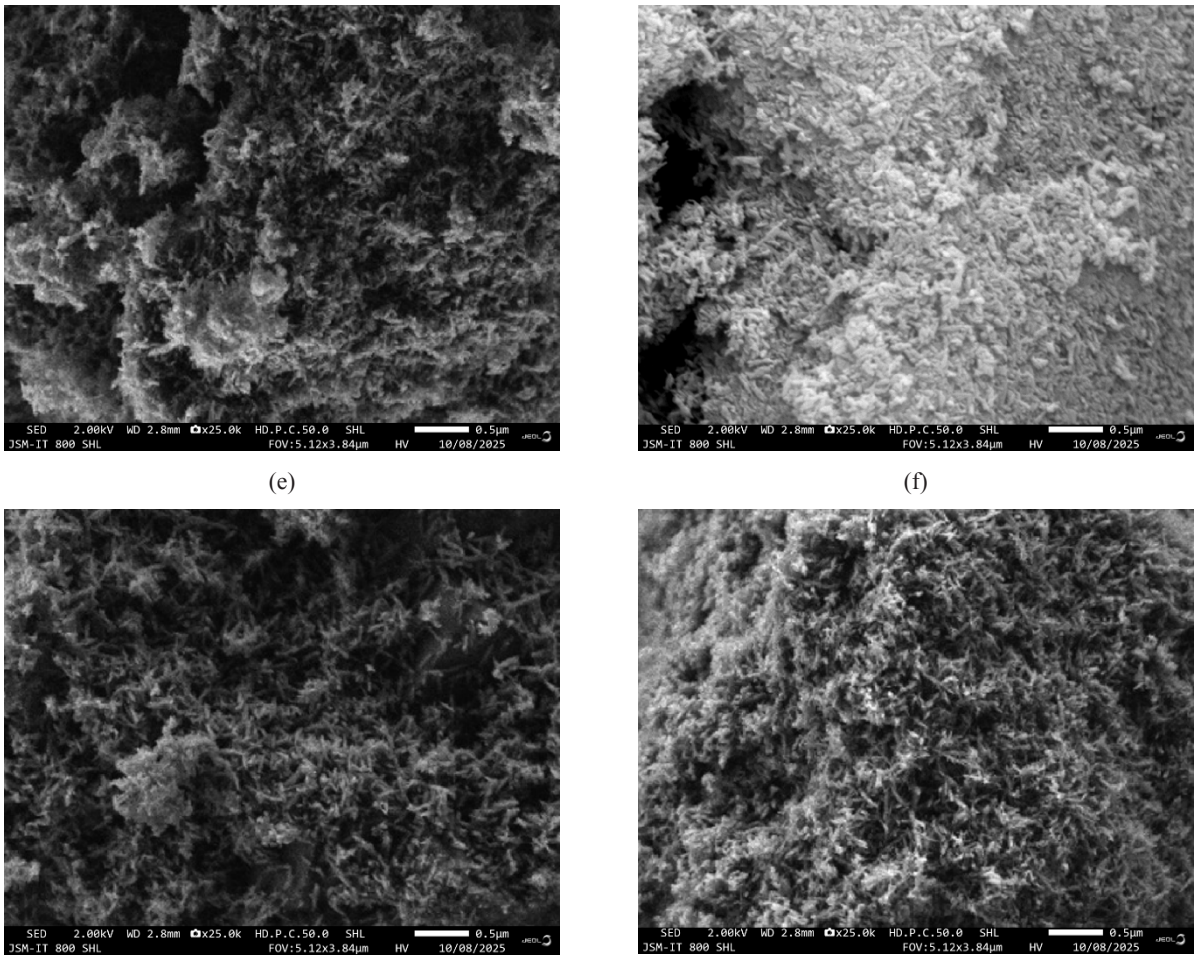


FIGURE 3. FESEM images for a) HA1, b) HA2, c) HA3, d) HA4, e) HA5, f) HA6, g) HA7 and h) HA8

TABLE 4. Average rod-like particle length measured from FESEM micrographs

Sample	Average particle length (µm)	Standard deviation (µm)
HA1	174.568	± 23.139
HA2	111.176	± 28.462
HA3	116.870	± 36.500
HA4	95.046	± 31.258
HA5	91.795	± 21.879
HA6	170.497	± 31.007
HA7	72.159	± 21.581
HA8	121.212	± 35.098

EDX ANALYSIS

The Ca/P ratios of the synthesized HA samples varied with the $CaCO_3$ source, pH value, and sintering condition as shown in Table 5. HA samples derived from *Corbicula Fluminea* shells exhibited Ca/P ratios ranging from 1.42 to 1.51 which are consistently lower than the stoichiometric HA value of 1.67. These values indicate the formation of calcium-deficient HA. Such calcium deficiency is commonly associated with the partial substitution of PO_4^{3-} groups by CO_3^{2-} ions within the HA lattice. This interpretation is supported by the FTIR results which revealed CO_3^{2-} absorption bands characteristic of B-type carbonated HA. Furthermore, the relatively low crystallinity observed in several Corbicula fluminea-derived samples by XRD suggests that carbonate incorporation increased

lattice disorder and reduced long-range crystal order.

In contrast, the Ca/P ratios of HA synthesized from *Pholas Orientalis* shells ranged from 1.59 to 2.13. Values exceeding the stoichiometric ratio of 1.67 suggest the presence of excess calcium or a deficiency of CO_3^{2-} during the synthesis process. The highest Ca/P ratio was observed for HA8 (2.13), which was synthesized at pH11 and subsequently sintered at 500°C. FTIR analysis of this sample showed relatively strong CO_3^{2-} absorption bands together with weaker CO_3^{2-} bands indicating possible CO_3^{2-} substitution and reduced PO_4^{3-} incorporation. However, despite the elevated Ca/P ratio, the XRD patterns did not show any identifiable diffraction peaks corresponding to secondary calcium-containing crystalline phases such as CaO or $CaCO_3$. Instead, HA8 exhibited the highest crystallinity value (51.47%), suggesting that the HA crystal structure remained largely intact. Therefore, the elevated Ca/P ratio is more likely associated with localized calcium enrichment, phosphate deficiency or calcium-rich domains below the XRD detection limit rather than the formation of detectable secondary crystalline phases.

The effect of pH on the Ca/P ratio differed between the two shell sources. For HA derived from *Corbicula Fluminea* shells, increasing the pH from pH10 to pH11 resulted in a moderate increase in the Ca/P ratio suggesting that a more alkaline environment promoted calcium incorporation or reduced PO_4^{3-} incorporation during HA formation. A less pronounced trend was observed for *Pholas Orientalis*-derived HA. Nevertheless, the combination of pH11 and sintering at 500°C produced the highest Ca/P ratio in HA8. This increase may be attributed to partial PO_4^{3-} loss during thermal treatment, resulting in a relatively calcium-rich composition. The corresponding XRD results indicate that this compositional change did not significantly compromise the crystallinity of the HA phase while FESEM observations revealed a denser and more compact microstructure after sintering.

TABLE 5. The Ca/P ratio of the HA samples

Sample	HA1	HA2	HA3	HA4	HA5	HA6	HA7	HA8
Ca/P ratio	1.43	1.42	1.47	1.51	1.70	1.59	1.69	2.13

In detail, FESEM, XRD and EDX results collectively demonstrate that the synthesis parameters significantly influenced the structural, compositional and morphological properties of the synthesized HA. Samples exhibiting higher crystallinity generally showed more compact and refined microstructures after sintering. For example, HA2 and HA8 exhibited the highest crystallinity values of 51.10% and 51.47% respectively. While FESEM observations revealed denser particle arrangements and evidence of particle coalescence after thermal treatment. The increase in crystallinity is attributed to crystal growth and reduction of lattice defects during sintering, which simultaneously promotes particle densification and microstructural ordering (Trzaskowska et al. 2023; Aspera-Werz et al. 2024).

A relationship was also observed between particle morphology and crystallite development. Samples synthesized at pH11 generally exhibited smaller and more homogeneous rod-like particles than those synthesized at pH10. The finer particles observed in HA3, HA4, HA7 and HA8 suggest that increased alkalinity enhanced nucleation kinetics resulting in the formation of a larger number of nuclei and restricting excessive particle growth. This trend is consistent with the XRD results where pH11 samples exhibited larger average crystallite sizes than pH10 samples indicating that particle refinement at the microscale did not necessarily correspond to smaller coherent crystalline domains at the nanoscale. Instead, crystal growth occurred within individual particles while maintaining an overall finer particle morphology.

The EDX results further support the structural observations. Samples derived from *Corbicula Fluminea* shells exhibited lower Ca/P ratios (1.42–1.51), indicating calcium-deficient HA. Calcium-deficient HA is commonly associated with CO_3^{2-} substitution and a less ordered crystal structure which agrees with the FTIR results showing CO_3^{2-} incorporation and the comparatively lower crystallinity observed in some samples. In contrast, HA derived from *Pholas Orientalis* shells exhibited higher Ca/P ratios (1.59 to 2.13) suggesting the presence of excess calcium-containing phases or PO_4^{3-} deficiency. Interestingly, despite the higher CO_3^{2-} absorption observed in FTIR spectra, the *Pholas Orientalis*-derived HA maintained moderate crystallinity indicating that the level of CO_3^{2-} substitution was insufficient to significantly disrupt the long-range crystal order detected by XRD.

Collectively, the results suggest that crystallinity, morphology and composition are strongly interrelated. Sintering promoted crystal growth, lattice ordering and particle densification resulting in higher crystallinity and more compact morphologies. Meanwhile, variations in Ca/P ratio and CO_3^{2-} substitution influenced the structural order of the HA lattice and consequently affected crystallinity. Therefore, the combined FESEM, FTIR, XRD and EDX analyses demonstrate that both shell source and synthesis conditions govern the evolution of HA through

interconnected morphological, compositional and crystallographic changes. These relationships are important because they ultimately determine the biological and mechanical performance of HA for biomedical applications particularly in bone tissue engineering where particle morphology, crystallinity and Ca/P ratio are key factors influencing bioactivity and osteogenic response (Wu et al. 2024; Zhang et al. 2022).

CONCLUSION

HA synthesized from *Corbicula Fluminea* and *Pholas Orientalis* shells at different pH values (pH10 and pH11) and sintering conditions (without sintering and sintering at 500°C) was successfully characterized using FTIR, XRD, FESEM and EDX analyses. FTIR results confirmed HA formation and revealed stronger CO_3^{2-} substitution in HA derived from *Pholas Orientalis* shells. XRD analysis demonstrated that all synthesized samples crystallized in the hexagonal HA phase, with crystallinity values ranging from 36.74% to 51.47%. FESEM observations showed that increasing pH generally produced finer and more homogeneous particles, while sintering promoted particle densification and crystal growth. EDX analysis further showed that the Ca/P ratios were influenced by the shell source and synthesis conditions.

These findings demonstrate that the shell source, reaction pH and sintering process significantly affect the structural, compositional and morphological characteristics of hydroxyapatite. Since crystallinity, particle morphology and Ca/P ratio are important parameters influencing the biological behaviour and performance of HA reported in previous studies (Wu et al. 2024; Zhang et al. 2022) the synthesized materials show promising characteristics for potential biomedical applications. However, the present study was limited to physicochemical characterization and no biological or mechanical evaluations were conducted. Therefore, further investigations involving cytocompatibility, bioactivity, osteogenic response and mechanical performance are necessary before confirming the suitability of the synthesized HA for biomedical applications.

ACKNOWLEDGEMENT

The authors gratefully acknowledge the support of Universiti Sains Islam Malaysia and Universiti Malaysia Perlis for providing laboratory facilities and technical assistance.

DECLARATION OF COMPETING INTEREST

None.

REFERENCES

Aditya, S., Stephen, J. & Radhakrishnan, M. 2021. Utilization of eggshell waste in calcium-fortified foods and other industrial applications: A review. *Trends in Food Science & Technology* 115: 422–432. https://doi.org/10.1016/j.tifs.2021.06.047

Ahmed, H.Y., Safwat, N., Shehata, R., Althubaiti, E.H., Kareem, S., Atef, A., Qari, S.H., Aljahani, A.H., Al-Meshal, A.S., Youssef, M. & Sami, R. 2022. Synthesis of natural nano-hydroxyapatite from snail shells and its biological activity: Antimicrobial, antibiofilm, and biocompatibility. *Membranes* 12(4): 408. https://doi.org/10.3390/membranes12040408

Alam, M.K., Hossain, M.S., Kawsar, M., Bahadur, N.M. & Ahmed, S. 2024. Synthesis of nano-hydroxyapatite using emulsion, pyrolysis, combustion, and sonochemical methods and biogenic sources: A review. *RSC Advances* 14(5): 3548–3559. https://doi.org/10.1039/D3RA07559A

Aspera-Werz, R.H., Chen, G., Schilonka, L., Bouakaz, I., Bronne, C., Cobraiville, E., Nolens, G. & Nussler, A. 2024. Impact of particle size and sintering temperature on calcium phosphate gyroid structure scaffolds for bone tissue engineering. *Journal of Functional Biomaterials* 15(12): 355. https://doi.org/10.3390/jfb15120355

Awasthi, S., Pandey, S.K., Arunan, E. & Srivastava, C. 2021. A review on hydroxyapatite coatings for the biomedical applications: Experimental and theoretical perspectives. *Journal of Materials Chemistry B* 9(2): 228–249. https://doi.org/10.1039/D0TB02407D

Benataya, K., Lakrat, M., Elansari, L.L. & Mejdoubi, E. 2020. Synthesis of B-type carbonated hydroxyapatite by a new dissolution-precipitation method. *Materials Today: Proceedings* 31: S83–S88. https://doi.org/10.1016/j.matpr.2020.06.100

Bernache-Assollant, D., Ababou, A., Champion, E. & Heughebaert, M. 2003. Sintering of calcium phosphate hydroxyapatite Ca10(PO4)6(OH)2 I. Calcination and particle growth. *Journal of the European Ceramic Society* 23(2): 229–241. https://doi.org/10.1016/S0955-2219(02)00186-3

Bontempi, E., Sorrentino, G.P., Zanoletti, A., Alessandri, I., Depero, L.E. & Caneschi, A. 2021. Sustainable materials and their contribution to the Sustainable Development Goals (SDGs): A critical review based on an Italian example. *Molecules* 26(5): 1407. https://doi.org/10.3390/molecules26051407

Ebrahimi, S., Hanim, Y.U., Sipaut, C.S., Jan, N.b.A., Arshad, S.E. & How, S.E. 2021. Fabrication of hydroxyapatite with bioglass nanocomposite for human Wharton's-jelly-derived mesenchymal stem cell growing substrate. *International Journal of Molecular Sciences* 22(17): 9637. https://doi.org/10.3390/ijms22179637

Etinosa, P.O., Osuchukwu, O.A., Anisiji, E.O., Lawal, M.Y., Mohammed, S.A., Ibitoye, O.I., Oni, P.G., Aderibigbe, V.D., Aina, T., Oyebode, D. & Nwigbo, S.C. 2024. In-depth review of synthesis of hydroxyapatite biomaterials from natural resources and chemical regents for biomedical applications. *Arabian Journal of Chemistry* 17(12): 106010. https://doi.org/10.1016/j.arabjc.2024.106010

Fendi, F., Abdullah, B., Suryani, S., Usman, A.N. & Tahir, D. 2024. Development and application of hydroxyapatite-based scaffolds for bone tissue regeneration: A systematic literature review. *Bone* 183: 117075. https://doi.org/10.1016/j.bone.2024.117075

Hussin, M.S.F., Abdullah, H.Z., Idris, M.I. & Abdul Wahap, M.A. 2022. Extraction of natural hydroxyapatite for biomedical applications—A review. *Heliyon* 8(8): e10356. https://doi.org/10.1016/j.heliyon.2022.e10356

Golubevas, R., Stankeviciute, Z., Zarkov, A., Golubevas, R., Hansson, L., Raudonis, R., Kareiva, A. & Garskaite, E. 2020. Acrylate–gelatin–carbonated hydroxyapatite (cHAP) composites for dental bone-tissue applications. *Materials Advances* 1(6): 1675–1684. https://doi.org/10.1039/D0MA00498G

Guerfi, Z., Kribaa, O.K. & Djouama, H. 2024. Chemical-physical behavior of hydroxyapatite: A modeling approach. *Journal of the Mechanical Behavior of Biomedical Materials* 150: 106229. https://doi.org/10.1016/j.jmbbm.2023.106229

Hassanein, S., Hassan, I., Salah, D., Sayed, M. & Naga, S. 2024. Synthesis of nano-hydroxyapatite powder from trough clam shells (Mactridae) by wet precipitation method for biomedical applications. *Egyptian Journal of Chemistry* 67(6). https://doi.org/10.21608/ejchem.2023.236647.8647

Ho, H.X., Chong, T.F., Ng, W.L. & Lee, S.Y. 2024. The complete mitochondrial genome data of *Pholas orientalis* (Gmelin, 1791) from Malaysia. *Data in Brief* 55: 110581. https://doi.org/10.1016/j.dib.2024.110581

Hossain, M.S., Mahmud, M., Sultana, S., Bin Mobarak, M., Islam, M.S. & Ahmed, S. 2021. Coupled effect of particle size of the source materials and calcination temperature on the direct synthesis of hydroxyapatite. *Royal Society Open Science* 8(9): 210684. https://doi.org/10.1098/rsos.210684

Huang, J. & Zhang, R. 2022. The mineralization of molluscan shells: Some unsolved problems and special considerations. *Frontiers in Marine Science* 9: 874534. https://doi.org/10.3389/fmars.2022.874534

Jindapon, N., Klinmalai, P., Surayot, U., Tanadchangsaeng, N., Pichaiaukrit, W., Phimolsiripol, Y., Vichasilp, C. & Wangtueai, S. 2023. Preparation, characterization, and biological properties of hydroxyapatite from bigeye snapper (*Priancanthus tayenus*) bone. *International Journal of Molecular Sciences* 24(3): 2776. https://doi.org/10.3390/ijms24032776

Kalpana, M. & Nagalakshmi, R. 2023. Effect of reaction temperature and pH on structural and morphological properties of hydroxyapatite from precipitation method. *Journal of the Indian Chemical Society* 100(4): 100947. https://doi.org/10.1016/j.jics.2023.100947

Karalkeviciene, R., Raudonyte-Svirbutaviciene, E., Zarkov, A., Yang, J.-C., Popov, A.I. & Kareiva, A. 2023. Solvothermal synthesis of calcium hydroxyapatite via hydrolysis of alpha-tricalcium phosphate in the presence of different organic additives. *Crystals* 13(2): 265. https://doi.org/10.3390/cryst13020265

Lee, I.H., Lee, J.A., Lee, J.H., Heo, Y.W. & Kim, J.J. 2020. Effects of pH and reaction temperature on hydroxyapatite powders synthesized by precipitation. *Journal of the Korean Ceramic Society* 57(1): 56–64. https://doi.org/10.1007/s43207-019-00004-0

Liang, Q., Dong, J., Ren, J., Xiao, C. & Deng, C. 2024. Intensified cross-linking dramatically improved the mechanical properties of hydroxyapatite and cellulose composites for repairing bone segmental defects. *Materials Advances* 5(6): 2556–2569. https://doi.org/10.1039/D3MA00974B

Liu, P., Li, Z., Yuan, L., Sun, X. & Zhou, Y. 2021. Pourbaix-guided mineralization and site-selective photoluminescence properties of rare earth substituted B-type carbonated hydroxyapatite nanocrystals. *Molecules* 26(3): 540. https://doi.org/10.3390/molecules26030540

Lubojański, A., Zakrzewski, W., Samól, K., Bieszczad-Czaja, M., Świtała, M., Wiglusz, R., Watras, A., Mielan, B. & Dobrzyński, M. 2024. Application of nanohydroxyapatite in medicine—A narrative review. *Molecules* 29(23): 5628. https://doi.org/10.3390/molecules29235628

Mohd Noor, M.S., Mohd Afandi, N.N.A., Mohd Noor, A.-F. & Baba Ismail, Y.M. 2020. Effect of carbonate to phosphate molar ratios on the physico-chemical properties of carbonated hydroxyapatite nanopowder. *Journal of Engineering Science* 16(2): 101–110. https://doi.org/10.21315/jes2020.16.2.5

Noviyanti, A.R., Akbar, N., Deawati, Y., Ernawati, E.E., Malik, Y.T., Fauzia, R.P. & Risdiana. 2020. A novel hydrothermal synthesis of nanohydroxyapatite from eggshell-calcium-oxide precursors. *Heliyon* 6(4): e03655. https://doi.org/10.1016/j.heliyon.2020.e03655

Nowicki, D.A., Skakle, J.M.S. & Gibson, I.R. 2022. Potassium–carbonate co-substituted hydroxyapatite compositions: Maximising the level of carbonate uptake for potential CO2 utilisation options. *Materials Advances* 3(3): 1713–1728. https://doi.org/10.1039/D1MA00676B

Owuamanam, S. & Cree, D. 2020. Progress of bio-calcium carbonate waste eggshell and seashell fillers in polymer composites: A review. *Journal of Composites Science* 4(2): 70. https://doi.org/10.3390/jcs4020070

Rodríguez-Lugo, V., Karthik, T.V.K., Mendoza-Anaya, D., Rubio-Rosas, E., Villaseñor Cerón, L.S., Reyes-Valderrama, M.I. & Salinas-Rodríguez, E. 2018. Wet chemical synthesis of nanocrystalline hydroxyapatite flakes: Effect of pH and sintering temperature on structural and morphological properties. *Royal Society Open Science* 5(8): 180962. https://doi.org/10.1098/rsos.180962

Seyhan, S.A., Alkaya, D.B., Cesur, S., Oktar, F.N. & Gunduz, O. 2022. Preparation and characterization of pure natural hydroxyapatite derived from seashells for controlled drug delivery. *Journal of the Australian Ceramic Society* 58(4): 1231–1240. https://doi.org/10.1007/s41779-022-00739-w

Tao, S.-Y., Wang, F.-F., Naz, K., Lin, X.-J., Xu, X.-H., Zhao, Y.-C., Hu, X.-C., Liu, B., Cao, S.-P. & Guo, Z.-L. 2022. Nano-hydroxyapatite use in oral medicine: A review. *International Journal of Materials Science and Applications* 11(3): 62–65. https://doi.org/10.11648/j.ijmsa.20221103.11

Sousa, R., Antunes, C. & Guilhermino, L. 2008. Ecology of the invasive Asian clam *Corbicula fluminea* (Müller, 1774) in aquatic ecosystems: An overview. *Annales de Limnologie - International Journal of Limnology* 44(2): 85–94. https://doi.org/10.1051/limn:2008017

Torres, B., Pérez, A., García, P., Jiménez, P., Abrigo, K., Valencia, P., Ramírez, C., Pinto, M., Almonacid, S. & Ruz, M. 2024. Fish bones as calcium source: Bioavailability of micro and nano particles. *Foods* 13(12): 1840. https://doi.org/10.3390/foods13121840

Trzaskowska, M., Vivcharenko, V. & Przekora, A. 2023. The impact of hydroxyapatite sintering temperature on its microstructural, mechanical, and biological properties. *International Journal of Molecular Sciences* 24(6): 5083. https://doi.org/10.3390/ijms24065083

Wu, S.-C., Hsu, H.-C., Wu, W.-H. & Ho, W.-F. 2024. Enhancing bioactivity and mechanical properties of nano-hydroxyapatite derived from oyster shells through hydrothermal synthesis. *Nanomaterials* 14(15): 1281. https://doi.org/10.3390/nano14151281

Zhang, L., Lu, T., He, F., Zhang, W., Yuan, X., Wang, X. & Ye, J. 2022. Physicochemical and cytological properties of poorly crystalline calcium-deficient hydroxyapatite with different Ca/P ratios. *Ceramics International* 48(17): 24765–24776. https://doi.org/10.1016/j.ceramint.2022.05.126